JOURNAL OF CATALYSIS 153, 108–122 (1995)

Synthesis and Catalytic Properties of Eggshell Cobalt Catalysts for the Fischer–Tropsch Synthesis

Enrique Iglesia,*,[1] Stuart L. Soled,‡ Joseph E. Baumgartner,‡ and Sebastian C. Reyes‡

*Department of Chemical Engineering, University of California at Berkeley, Berkeley, California 94720; and ‡Corporate Research Laboratories, Exxon Research and Engineering Company, Route 22 East, Annandale, New Jersey 08801

Received August 11, 1994; revised November 7, 1994

CO diffusional restrictions decrease the rate and C_5^+ selectivity in large (1–3 mm) catalyst pellets required for Fischer–Tropsch synthesis in packed bed reactors. Eggshell catalysts, in which the active Co component is preferentially located near the outer pellet surface, decrease these transport restrictions and increase Fischer–Tropsch synthesis rates and C_5^+ selectivity. Maximum C_5^+ selectivities occur on catalysts with intermediate shell thickness, because these catalysts avoid intrapellet CO concentration gradients but still restrict the diffusive removal of reactive olefin products, which can readsorb and continue to grow to higher molecular weight hydrocarbons. Eggshell catalysts were prepared by a novel impregnation technique using molten cobalt nitrate. The eggshell thickness is controlled by the melt viscosity and by the contact time between the melt and the support pellet. These impregnation procedures and the slow reduction of the impregnated nitrate salts lead to relatively high cobalt dispersions (0.05–0.07) even at the high Co concentrations (40–50 wt%) present within the shell region. © 1995 Academic Press, Inc.

1. INTRODUCTION

We have previously reported that Fischer–Tropsch (FT) synthesis turnover rates on Co and Ru do not depend strongly on metal dispersion and metal oxide support (e.g., TiO_2, SiO_2, Al_2O_3, etc.) (1). Hydrocarbon product selectivity, however, depends on a complex interplay between diffusion, reaction, and convection processes occurring within catalyst pellets and reactors (1–5). At typical FT synthesis conditions, two types of reaction–diffusion coupling mechanisms become important: (a) diffusion-limited product removal from catalyst pellets and reactors and (b) diffusion-limited reactant arrival at catalytic sites. The first type leads to enhanced readsorption of α-olefins and to higher product molecular weight and paraffin content as the pellet size or the active site density increase. In the second regime, catalyst pellets become depleted of CO as transport restrictions become more severe. This leads to low intrapellet CO concentrations, which favor the formation of lighter products and decrease C_5^+ selectivity. Consequently, maximum C_5^+ selectivities are observed for intermediate levels of transport restrictions.

Packed-bed FT reactors require large pellets (1–3 mm) in order to maintain acceptable pressure gradients; they also require very active pellets in order to minimize reactor volumes required to achieve a given conversion. These requirements often lead to transport restrictions in many applications of FT synthesis. Here, we describe how SiO_2 pellets containing non-uniform radial distributions of Co sites can decouple the pellet size from the characteristic diffusion distance. We also describe the synthesis and catalytic behavior of pellets with even and eggshell active site distributions (6–8). The concepts and models described for Co catalysts here also apply to FT synthesis on Ru and Fe. Our work provides experimental evidence and a strong theoretical framework for the optimal design and the efficient use of eggshell catalysts in transport-limited FT synthesis reactions.

2. BACKGROUND

2.1. Transport Effects in Fischer–Tropsch Synthesis

Many studies have examined the role of transport in FT synthesis reactions. Fischer and Tropsch (9) reported higher synthesis rates and C_5^+ selectivity on smaller Fe catalyst pellets. Anderson *et al.* (10) attributed similar results to CO and H_2 diffusional restrictions, which decreased the kinetic driving force for FT synthesis. A dimensional analysis of a simplified reaction-transport model suggested that pellets smaller than about 0.2 mm diameter are required in order to avoid transport restrictions for typical FT synthesis conditions and reaction rates (11).

Intraparticle reactant gradients were neglected in previous FT synthesis modeling studies (12, 13), even though transport limitations occur on pellets as small

[1] To whom correspondence should be addressed.

0021-9517/95 $6.00

as 0.3 mm (14). Some models have included intrapellet transport restrictions in order to describe the behavior of large Ru pellets, but at synthesis conditions at which catalyst pores do not contain liquid reaction products (15, 16). More recent studies also describe intrapellet diffusion–reaction processes for packed-bed (17, 18) and slurry (13) reactors but include only H_2 concentration gradients, even though CO is the diffusion-limited reactant in FT synthesis using stoichiometric feeds. These models account for the decrease in synthesis rate and activation energy observed on Co catalysts as pellet size increases; they do not, however, describe the marked effects of reactant or product intrapellet gradients on FT synthesis selectivity.

Recently, we have developed reaction-transport models that account for transport effects on selectivity (1, 3, 4, 19). Synthesis rates and C_5^+ selectivities ultimately decrease with increasing pellet size or volumetric site density because intrapellet CO concentrations decrease as reaction rates become limited by diffusion.

The use of eggshell catalysts to avoid diffusional restrictions in FT synthesis reactions has been reported previously (19–25); eggshell catalysts were proposed even earlier as a way to improve the rate and selectivity of diffusion-limited catalytic reactions (6–8). The use of eggshell catalysts in FT synthesis becomes important because of the inherent transport limitations reported in early studies of this reaction (9, 10). In fact, eggshell Ru catalysts were intentionally used in early FT synthesis studies (26) and, perhaps inadvertently in several other studies, in which certain impregnation and pretreatment techniques may have led to nonuniform distributions with higher metal concentrations near outer pellet surfaces.

2.2. Nonuniform Distributions of Active Components in Catalytic Pellets

Kasoaka and Sakata (27) first suggested the benefits of nonuniform catalyst activity (and site density) on catalytic reactions, after the first successful preparation of intentionally nonuniform catalysts by Maatman and Prater (6). Model descriptions of nonuniformly impregnated catalysts were later extended to general pellet geometries and activity profiles [28] and applied to the analysis of specific catalytic reactions (29–31). Previous experimental and theoretical studies have been recently summarized by Lee and Aris (32).

Four different types of distributions of active components can occur in supported catalysts: uniform, eggshell, eggyolk, and eggwhite. They contain active species evenly distributed or selectively deposited near the pellet outer surface, pellet center, or intermediate pellet regions, respectively (6, 7). Impregnation, drying, and pretreatment steps during catalyst preparation determine the type of distribution. Convection, diffusion, and adsorption processes during impregnation and drying control the penetration depth and the local concentration of impregnants within pellets. As a result, the adsorption strength of precursors and the contact time between pellets and solutions are critical parameters in impregnation processes. When adsorption is weak, impregnated species reequilibrate quickly during drying and pretreatment and typically lead to uniform distributions of active components. Strongly adsorbing species usually lead to eggshell or eggwhite configurations.

Early studies of intrapellet metal distributions focused on Pt-based catalysts used in diffusion-limited oxidation reactions. Eggshell CO oxidation catalysts can be prepared by impregnating Al_2O_3 supports with a H_2PtCl_6 solution (33, 34), in a process involving rapid and strong adsorption of the Pt complex onto alumina. Eggwhite Pt catalysts can be prepared by impregnation with solutions containing picric acid, followed by acid washing (0.1 *M* HCl) and drying (33). $Pt(NH_3)_4(NO_3)_2$ complexes adsorb more weakly than H_2PtCl_6 and form radially uniform Pt distributions (34).

Here, we report a new technique for the synthesis of eggshell catalysts with sharply defined outer shell regions. This technique exploits the controlled penetration of a molten salt as it contacts a porous support pellet. We provide specific examples of its use in the synthesis of supported Co-based FT synthesis catalysts. Our technique offers a practical method for the synthesis of high-metal loading eggshell catalysts, even for systems where weak impregnant-support interactions preclude the use of controlled adsorption methods.

3. EXPERIMENTAL

3.1. Catalyst Preparation

Capillary imbibition rates of cobalt-containing aqueous solutions of cobalt nitrate melts (at 333 and 348 K) were measured by attaching individual SiO_2 spheres (Shell S980B, 210 $m^2\ g^{-1}$, 2.7 mm diameter, precalcined at 873 K) to the end of wooden applicator sticks using an epoxy resin. Aqueous cobalt nitrate solutions were prepared by dissolving 0.5 g cobalt nitrate/cm^3 of H_2O (Solution A), and by adding 1.0 wt% hydroxyethylcellulose (Solution B) to increase the viscosity of Solution A to that of the cobalt nitrate melt. Another solution (Solution C), with much lower Co nitrate concentration (0.01 g/cm^3), was prepared in order to examine the behavior of very dilute solutions.

Silica spheres were immersed in selected solutions and melts for 2, 4, 8, 16, 32, or 48 s. These immersion experiments were repeated using preheated (383 K) or cooled

(263 K) spheres in order to examine the effect of melt thickening or thinning during nonisothermal capillary imbibition. For each measurement, 10 spheres were individually immersed for a given time, the excess liquid was removed by wiping their surface, and the samples were dried in air for 0.5 h. The samples were then calcined in air at 623 K for 0.25 h to form Co_3O_4, which allowed sharp visual contrast in optical microscopy measurements. A Nametre vibrating sphere viscometer, calibrated using Cannon standards, was used to measure the solution and melt viscosities. Surface tensions were measured with a Kruss K-10 tensiometer using the ring method.

Eggshell and uniformly impregnated Co/SiO_2 catalysts were prepared for FT evaluation using several impregnation techniques. Evenly impregnated Co/SiO_2 powders (0.143 mm average pellet diameter) were prepared by contacting an acetone/SiO_2 slurry (Davison 62, W. R. Grace Co., 280 $m^2\ g^{-1}$, calcined 873 K) with a solution of Co nitrate ($Co(NO_3)_2 \cdot 6H_2O$, Alfa) in acetone. Large uniform Co/SiO_2 pellets were prepared by incipient wetness impregnation of silica spheres (Shell S980G; 115 $m^2\ g^{-1}$, 2.2 mm pellet diameter, calcined 873 K, 16 h) with an aqueous Co nitrate solution. A similar sample, prepared by uniform impregnation of higher surface area SiO_2 spheres (Shell S980B; 1.7 mm pellet diameter, 260 $m^2\ g^{-1}$), was crushed and sieved to form pellets with diameters between 0.125 and 1.7 mm; these samples were used to determine the effect of the characteristic diffusion distance (pellet radius) on FT synthesis rates and selectivity.

Eggshell catalysts were prepared by placing SiO_2 spheres (S980G, 2.2 mm pellet diameter, 12.5 g) into a fritted glass funnel (5.5 cm diameter) containing 15–20 mm layers of 6 mm nonporous glass beads next to the fritted bottom. Both the impregnant viscosity and imbibition contact time were controlled. Molten Co nitrate (~50 g, melting point ~323 K) at 348–363 K was poured uniformly over the SiO_2 spheres (2–3 cm bed height). The bed was stirred with a glass rod, and vacuum was used to remove the molten nitrate rapidly from the bed within 2–4 s. The samples were then dried in air at 383 K for 2 h. Comparative samples were also prepared using this short contact time technique but with an aqueous Co nitrate solution (Solution A, Table 1) at room temperature (RT) instead of the nitrate melt.

All catalysts were directly reduced in flowing H_2 by increasing the temperature from 373 K to 693–723 K at 6–12 K h^{-1} and then holding at 693–723 K for 4–16 h. Samples were passivated by contact with a dilute oxygen stream (1% O_2/He) at RT before exposing them to air. Passivated catalysts were re-reduced at 693–723 K for 2–4 h before catalytic and chemisorption measurements. A portion of these eggshell and evenly impregnated pellets was crushed and sieved to obtain pellets with 0.143 mm average diameter.

TABLE 1

Properties of Impregnating Nitrate Solutions and Melts

Impregnating liquid	Hydroxyethyl-cellulose (HEC, wt%)	Viscosity (μ, cP)	Surface tension (γ, dyne cm^{-1})
Solution A[a]	0	3.2 (298 K)	65.6
Solution B[a]	1.0	45 (298 K)	66.4
Melt	0	48 (333 K)	—
Melt	0	31 (348 K)	66.2
Solution C[b]	0	0.93 (298 K)	66.9
Water	0	0.92 (295 K)	70.6

[a] 0.5 g Co nitrate/cm^3 H_2O.
[b] 0.01 g Co nitrate/cm^3 H_2O.

3.2. Catalyst Characterization

All catalysts were characterized by X-ray diffraction, hydrogen chemisorption, nitrogen physisorption, and optical microscopy. The Co content was measured by atomic absorption or by gravimetric measurements of weight loss during catalyst reduction and oxidation processes.

X-ray diffraction was used to determine Co crystal structures formed during synthesis, pretreatment, and catalytic tests. Average crystallite diameters were estimated from the breadth of diffraction lines using the Scherrer equation. Measurements were carried out in a Phillips 3000 APD diffractometer using Cu$K\alpha$ radiation and a scintillation counter detector. Support surface area and pore size distributions were measured by nitrogen physisorption and capillary condensation methods using the BET and Kelvin equations (35).

Cobalt dispersion was measured by hydrogen chemisorption at 373 K assuming a 1 : 1 H : Co surface stoichiometry (20); these measurements were carried out in a glass volumetric adsorption unit capable of 2×10^{-4} Pa dynamic vacuum. Passivated samples were re-reduced at 623 K for 1–2 h, evacuated to less than 10^{-3} Pa for 0.5–1.0 h at 523–623 K, and cooled to 373 K, where chemisorption isotherms were measured at five H_2 pressures between 15 and 80 kPa. These isotherms were extrapolated to zero pressure in order to calculate total chemisorption uptakes.

The thickness of the outer shell was determined by optical microscopy on impregnated samples calcined at 623 K for 0.25 h. The spheres were split with a razor blade and the two halves mounted with their flat surface down onto a glass slide using a clear non-penetrating epoxy. Internal pellet surfaces were exposed by sanding in a Buehler polishing wheel using fine (600 grit) polishing paper. Micrographs were obtained using a Leitz optical microscope equipped with a Polaroid camera and a 0.05 mm resolution calibrated grid. The thickness

of the shell regions was measured with an accuracy of 0.01 mm.

3.3. Catalytic Experiments

FT synthesis rates and selectivities were measured in an isothermal packed-bed reactor at 473 K and 2000 kPa, using stoichiometric feeds (H_2/CO = 2.0–2.1). Catalysts were mixed with quartz powder (0.1–0.2 mm diameter) in order to avoid local exotherms and the channeling or bypassing that can occur when large catalyst pellets (>1 mm) are used in small diameter (~1 cm) reactors.

Passivated catalysts were re-reduced in flowing H_2 at 623 K, cooled to 473 K, and exposed to reactants. All reported data were obtained after at least 24 h on stream in order to ensure steady-state behavior and representative product samples. Light products (CO, CO_2, C_1–C_{15}) were analyzed by on-line gas chromatography (with N_2 as internal standard) using thermal conductivity, flame ionization, and mass spectrometric detection (1). C_{15}–C_{500} products were collected as liquids and analyzed by high-temperature gas chromatography and gel-permeation chromatography (1).

Reaction rates are reported as cobalt-time yields (molar CO conversion rate per g atom Co) and site-time yields (molar CO conversion rate per g atom surface Co). Selectivities are reported as the percentage of reacted CO that appears as a given product. The reported chain growth probabilities (α) are constant asymptotic values obtained for C_{15}–C_{50} products, a carbon number range where α becomes independent of chain size (1–5).

3.4. Liquid Imbibition into Porous Pellets

The impregnation of catalyst supports with metal salt solutions has been widely studied because of its industrial importance (42). Here, we are concerned primarily with the processes controlling the rate of imbibition of an impregnating solution into a porous support pellet.

The synthesis of thin eggshell regions requires accurate control of the penetration depth and of the uniformity of the advancing liquid front. Available models predict the location of the liquid front in a single capillary as a function of the imbibition time (32). The complex pore morphology of the support (i.e., pores of varying size, shape, and orientation) precludes, however, rigorous mathematical descriptions. Additional uncertainties are introduced by the lack of adequate models describing impregnant-support interactions.

Following the analysis of Washburn (36), it can be shown that the position of the liquid front r^* within a single capillary pore is controlled by the following liquid and solid properties: liquid viscosity (μ) and surface tension (γ), support pore radius (r_p) and pellet radius (R_0), the tortuosity of the pore structure (τ), and the contact angle between the liquid and the support surface (θ). The dimensionless penetration depth ($\zeta = r^*/R_0$) can be estimated by

$$\zeta = \Omega \cdot t^{1/2} \quad [1]$$

where

$$\Omega = \left[\frac{1}{\tau \cdot R_0^2} \cdot \frac{\gamma \cdot r_p \cdot \cos(\theta)}{2 \cdot \mu}\right]^{1/2}. \quad [2]$$

These equations are strictly applicable to (tortuous) cylindrical capillaries. As an approximation, they can also be used to describe small penetration depths in spherical particles. They do not account for build-up of internal pressure by trapped air or for curvature effects in spherical pellets. Eq. [1] suggests that a plot of ζ vs $t^{1/2}$ gives a straight line with slope Ω. A priori estimates of Ω require that we measure γ, r_p, θ, and μ accurately. We show below that, within the above assumptions, Eqs. [1] and [2] provide an adequate description of liquid motion within capillary networks in our support pellets.

4. RESULTS AND DISCUSSION

4.1. Catalyst Synthesis and Characterization

The effects of viscosity, surface tension, and pore structure on liquid penetration rates were determined by immersing individually mounted silica spheres (2.7 mm diameter, 210 $m^2\ g^{-1}$) into cobalt nitrate melts and solutions (Fig. 1a). Hydroxyethyl-cellulose (HEC) was added to some solutions to increase their bulk viscosity to values similar to those of nitrate melts. For example, the bulk viscosity of Solution B (0.5 g Co nitrate/cm^3 H_2O, 1 wt% HEC) at room temperature was 45 cP, similar to that of nitrate melts (48 cP at 333 K) (Table 1). The surface tension of nitrate solutions was not strongly affected by temperature or by the presence of HEC and resembles values obtained for nitrate melts (Table 1).

The penetration rate of nitrate melts (at 333 K) into silica spheres (2.7 mm diameter, 210 $m^2\ g^{-1}$) is much slower than that of nitrate solutions of similar viscosity and surface tension at room temperature (Solution B, Fig. 1a(ii); 1a: curves C and B, Fig. 2). Both liquids, however, penetrate silica spheres more slowly than aqueous nitrate solutions without HEC (Solution A, Fig. 1a(i) and curve A in Fig. 2). Melt imbibition rates into silica spheres heated (383 K) or cooled (263 K) before immersion resemble those on spheres held at RT. Apparently, the viscosity of melts as they penetrate a colder porous sphere is similar to that of the bulk liquid because rapid thermal equilibration occurs between the spheres and the melt. This was confirmed by dimensional analysis and numerical simulations using a non-isothermal liquid imbibition model.

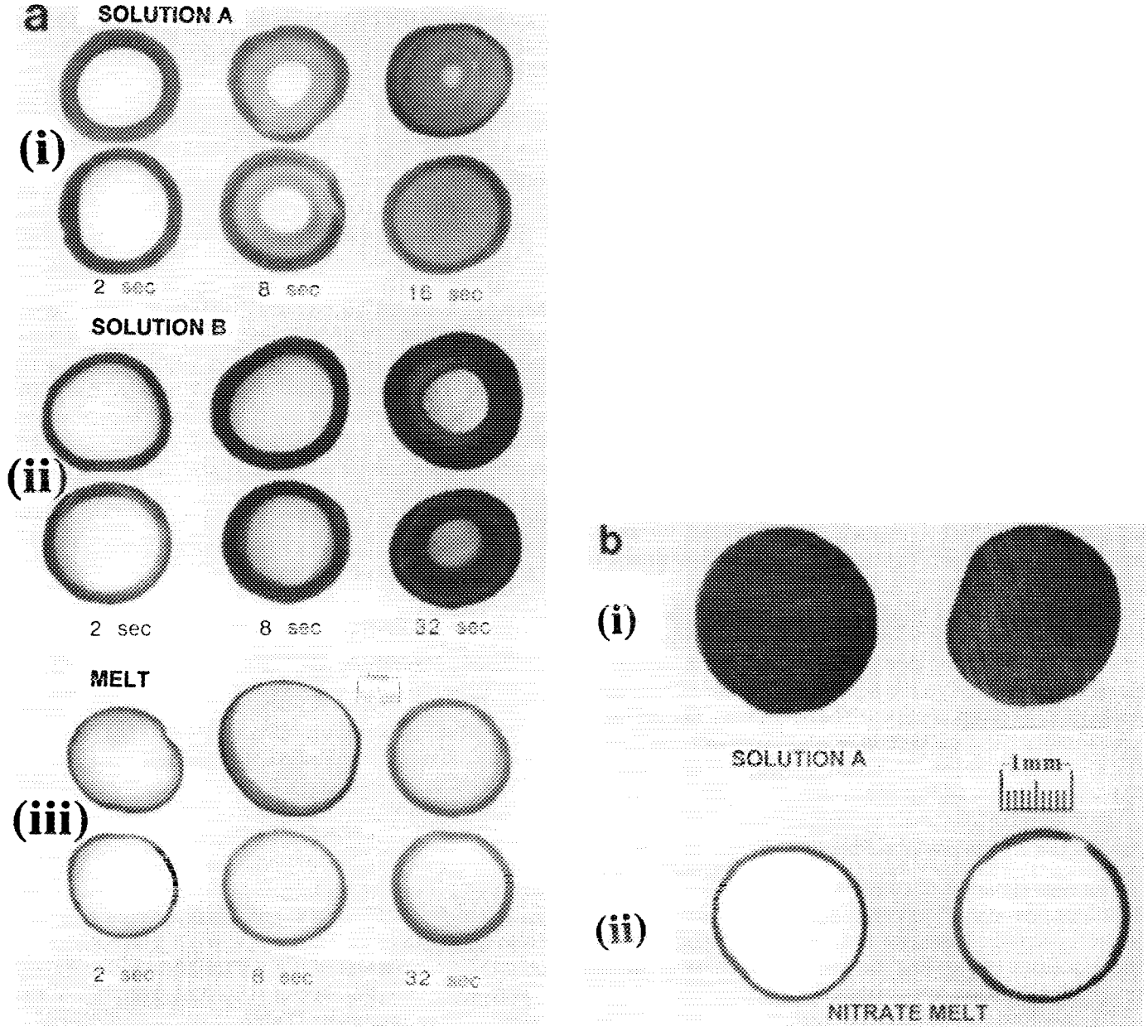

FIG. 1. Optical micrographs of eggshell Co/SiO_2 catalysts (contact times of 1–5 s, 353 K melt; 293–298 K solutions and spheres). (a) controlled immersion method using (210 $m^2 g^{-1}$, 2.7 mm diameter). (i) aqueous solution (Solution A); (ii) viscosified aqueous solution (Solution B) (iii) melt. (b) vacuum filtration method using (115 $m^2 g^{-1}$, 2.2 mm diameter). (i) aqueous solution (Solution A), (ii) melt.

For melt impregnants, the shell thickness was less than 0.20 mm even for contact times as long as 30 s (Fig. 1a(iii); curve C, Fig. 2). Increasing contact times led to thicker shells and the liquid ultimately penetrated the entire sphere. The slower penetration of nitrate melts was also observed on lower surface area silica spheres (Fig. 3).

In Figs. 2 and 3, liquid penetration depths are plotted against $t^{1/2}$, as suggested by Eq. [1]. Table 2 shows the slopes of the linear region in such curves and those calculated from Eq. [2] using measured pore structure and solution properties, perfect wetting of solid surfaces by the liquid ($\theta = 0$), and a pellet tortuosity value of 1.8 (39). The agreement between theoretical and experimental values is excellent for nitrate melts and solutions; experimental penetration rates differ significantly from theoretical predictions only for viscosified nitrate solutions. The latter solutions penetrate significantly faster than predicted by the imbibition model. This suggests that the

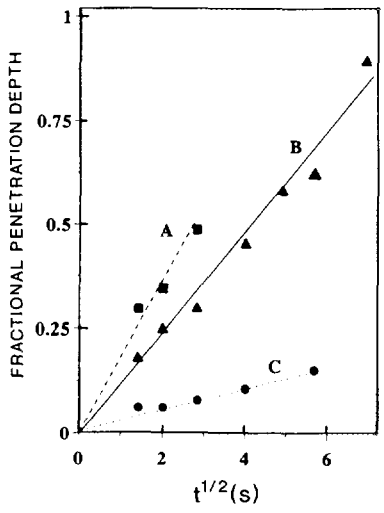

FIG. 2. The effect of impregnating solution on liquid penetration depth (eggshell thickness) (SiO_2, 210 m^2 g^{-1}, 2.7 mm diameter; Curve A—Solution A (298 K); Curve B—Solution B (298 K); Curve C—nitrate melt (333 K)).

solution viscosity within pellet pores is much lower than in the bulk liquid. Energy dispersive electron microscopy shows that when 1% HEC impregnated pellets are pyrolyzed at 637 K in N_2 for 12 h, the HEC additive remains on the external pellet surfaces during imbibition. As a result, the effective viscosity of the intrapellet liquid is much lower than the surrounding bulk liquid.

Catalyst surface area, cobalt dispersion, and average shell thickness are shown in Table 3 for all samples. Cobalt dispersions are between 0.050 and 0.063. The cobalt dispersions in eggshell catalysts are similar to those observed in even pellets or powders, in spite of the much higher Co concentrations within shell regions in the eggshell samples. These cobalt dispersions, however, require the direct reduction of nitrate salts in hydrogen at a very slow heating rate (<12 K h^{-1}) and the elimination of intermediate calcination steps (25, 37, 38).

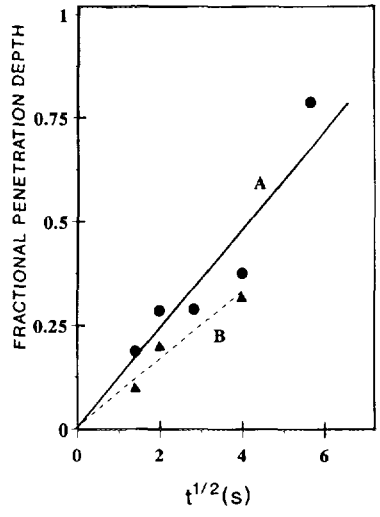

FIG. 3. The effect of impregnating solution on liquid penetration depth (eggshell thickness) (SiO_2, 110 m^2 g^{-1}, 2.2 mm diameter; Curve A—Solution B (RT); Curve B—nitrate melt (333 K)).

4.2. Catalytic Behavior of Even and Eggshell Pellets

Our melt impregnation technique allows the synthesis of eggshell catalysts with Co sites located within 0.1–0.2 mm of outer pellet surfaces (Fig. 1b(ii)). These samples were prepared by contacting a bed of silica spheres (2.2 mm, 115 m^2 g^{-1}) (with molten Co nitrate (348–363 K) for 2–4 s using the vacuum filtration technique. The resulting materials contain 10–13 wt% cobalt. The local Co content in the shell area is 40–50 wt% and about 75% of the pellet volume contains no Co crystallites. Similar vacuum filtration techniques using aqueous Co nitrate solutions (Solution A) instead of melts lead to complete penetration of the impregnating solution into the silica spheres, even at contact times shorter than 5 s (Figure 1b(i)).

FT synthesis rates and selectivities are shown in Table 3 and Fig. 4. Large, uniformly impregnated pellets (2.2 mm diameter) give lower cobalt-time yields (Fig. 4a), higher CH_4 selectivies (Fig. 4b), and lower activation energies (68 ± 8 kJ mol^{-1}) than similar Co/SiO_2 powders with much smaller pellet diameters (115 ± 6 kJ mol^{-1}, 0.143 mm). FT synthesis rates, C_5^+ selectivities, and activation energies increase when large pellets are crushed and sieved to retain particles with 0.143 mm average diameter (Table 3). This suggests that catalytic rates within large pellets are inhibited by slow reactant (CO) arrival at reaction sites and are well below intrinsic rate values.

Similar improvements in synthesis rate and C_5^+ selectivity were obtained by placing Co sites within 0.1 mm of outer pellet surfaces. These eggshell catalysts are more active and selective for C_5^+ synthesis than uniformly impregnated large pellets (Table 3, Fig. 4). Cobalt-time yield and C_5^+ selectivity become slightly higher when these eggshell catalysts are crushed to form 0.143 mm diameter pellets. Therefore, reaction rates remain partially limited by reactant arrival even on these eggshell catalysts.

The methane selectivity and the olefin content of synthesis products are also affected by transport restrictions. The olefin content is higher on small or partially impregnated pellets (Table 3) than on large uniform pellets, suggesting that low intrapellet CO concentrations caused by diffusional restrictions increase the rate of secondary olefin hydrogenation reactions. Large pellets increase intrapellet olefin concentrations, which also lead to higher secondary hydrogenation and readsorption rates. Methane selectivity decreases as CO transport restrictions are

TABLE 2

Liquid Penetration Rates: Comparison of Experimental Values and Model Predictions

Impregnating liquid/solution	Liquid temperature (K)	Sphere diameter ($2 \cdot R_0$, cm)	Average pore radius (r_p/nm)	Slope[a] (experimental)	Slope[b] (model)
A	298	0.27	8.5	0.18	0.16
B	298	0.27	8.5	0.12	0.045
Melt	298	0.22	16.0	0.12	0.075
Melt	333	0.27	8.5	0.028	0.042
Melt	333	0.22	16.0	0.085	0.074
Melt (Silica at 383K)	348	0.27	8.5	0.035	0.052
Melt (Silica at 263K)	348	0.27	8.5	0.41	0.052
C	298	0.27	8.5	0.29	0.31

[a] From slope of ζ vs $t^{1/2}$ plots.
[b] From Eq. [1]; slope = $[(1/\tau) \cdot R_0^2 \cdot (\gamma \cdot r_p \cdot \cos(\theta)/2 \cdot \mu)]$; $\tau = 1.8$ [39]; $\theta = 0$.

removed, whether their removal occurs by partial impregnation or by decreasing pellet size (Table 3), because both procedures decrease the distance over which reactants must diffuse to reach catalytic sites.

Two results shown in Table 3 may appear surprising at first. Yet, they are consistent with transport effects predicted by previously developed reaction-transport models (1, 3, 4). First, C_5^+ selectivities are actually higher on crushed eggshell catalysts than on crushed even pellets or Co/SiO_2 powders, even though FT syn-

TABLE 3

Catalyst Characterization and Fischer–Tropsch Synthesis Data on Co/SiO_2 Powders and Even and Eggshell Large Pellets

	Co/SiO_2, (12.7–13.1% Co wt.)				
Catalyst	Uniformly impregnated large pellet	Crushed large pellet	Eggshell pellet	Crushed eggshell pellet	Small pellet
Co site density ($10^6 \cdot$ g atom surface Co $\cdot$ m^{-2})	0.21	1.21	1.03 (3.6[a])	1.03 (3.6[a])	0.38
Pellet size (mm)	2.2	0.17	2.2	0.17	0.17
Silica surface area (m^2 g^{-1})	115	115	115	115	280
Average pore diameter (nm)	32	32	32	32	13.5
Impregnated pellet region (average eggshell thickness or pellet diameter) (mm)	2.2	0.17	0.23	0.17	0.17
Characteristic diffusion length (mm)	1.1	0.085	0.23	0.085	0.085
Structural parameter[b] χ(m^{-1} × 10^{-16})	21960	136	1908	272	95
Site-time yield (h^{-1})	50	95	105	140	110
Cobalt-time yield (h^{-1})	3.15	5.98	5.78	5.45	5.50
CH_4 selectivity (%)	12.1	5.2	7.7	4.7	7.0
C_5^+ selectivity (%)	81.5	89.6	88.0	90.5	83.5
CO_2 selectivity (%)	0.90	0.18	0.50	0.16	0.15
Activation energy/kJ mol^{-1}	68	—	—	—	115
Propylene/propane ratio	0.20	2.6	0.50	2.7	2.9
1-butene/*n*-butane ratio	0.11	1.7	0.32	1.8	2.7

Note. 473 K, 2000 kPa, $H_2/CO = 2.1$, 55–65% CO conversion, >24 h on stream.
[a] Within impregnated shell region.
[b] $\chi = L_2 \Phi \theta / r_p$; r_p in m, site density (θ) in Co atoms/m^2, L as twice the characteristic diffusion distance in m.

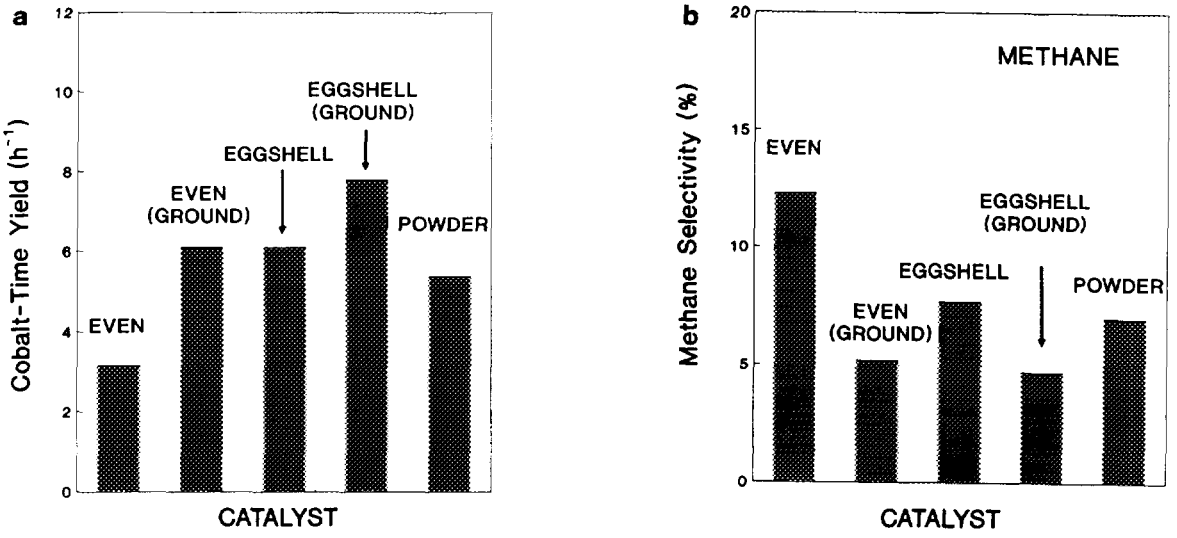

FIG. 4. Fischer–Tropsch synthesis rate (a) and CH_4 selectivity (b) on Co/SiO_2 powders and even and eggshell pellets. (473 K, 2000 kPa, H_2/CO = 2.1, 55–65% CO conversion, >24 h on stream; rate expressed as Co-time yield, the molar CO conversion rate per g atom Co.)

thesis is not affected by reactant transport on any of these samples. These differences arise from the higher local site densities present in ground eggshell catalysts, where all the Co sites are located within fragments formed from impregnated shell regions. Local Co site densities are about four times greater than in crushed even samples and about 20 times greater than in Co/SiO_2 powders with lower site density and higher support surface area. As a result, the readsorption probability of reactive olefins, a reaction that initiates surface chains and leads to higher molecular weight products, is significantly greater on powders formed from eggshell pellets (1–4).

The second observation involves the apparent transport restrictions observed on catalysts with 0.23 mm eggshell thickness (Table 3). Their eggshell thickness is only slightly larger than the diameter of crushed eggshell or powder catalysts (0.17 mm). Access to the eggshell region, however, occurs only from one side of the impregnated shell. Also, the slab geometry of the thin shell maintains a nearly constant number of sites as the distance from the surface increases and the local site density is much greater than on powders with similar overall Co content. These factors combine to slow down CO transport and to increase the transport load required to maintain intrinsic rates and high intrapellet CO concentrations. As a result, C_5^+ selectivities on these eggshell catalysts remain lower than on crushed eggshell samples. These observations and their use in the FT synthesis catalysts are discussed in Section 4.5, where we describe the role of catalyst structure in the control of transport rates within FT synthesis pellets.

4.3. Pellet Diameter Effects on Fischer–Tropsch Synthesis Rate and Selectivity

Pellet diameter effects on synthesis rate and selectivity were determined by measuring the catalytic behavior of Co sites uniformly distributed within SiO_2 pellets (24.8 wt% Co) of 0.13, 0.165, 0.36, 0.86, and 1.5 mm average diameter. These catalysts were prepared by crushing a single batch of evenly impregnated silica spheres (1.7 mm diameter, 260 $m^2\ g^{-1}$). Therefore, volumetric catalyst rates and structural properties, except pellet diameter, were identical in all samples.

TABLE 4

Pellet Diameter Effects on Fischer–Tropsch Synthesis Rate and Selectivity

Pellet diameter (mm)	0.13	0.165	0.36	0.86
Characteristic diffusion distance (mm)	0.065	0.0825	0.18	0.425
Structural parameter[a] χ ($m^{-1} \times 10^{-16}$)	70	22	536	2988
Co-time yield (h^{-1})	4.30	3.99	4.90	3.98
Site-time yield (h^{-1})	110	102	105	102
CH_4 selectivity (%)	8.1	6.6	5.9	8.7
C_5^+ selectivity (%)	81.0	82.3	87.1	82.0
CO_2 selectivity (%)	0.20	0.22	0.45	0.80
(1-hexene/*n*-hexane) ratio	1.25	1.10	1.03	0.20

Note. 474 K, 2000 kPa, H_2/CO = 2.08, 60–65% CO conversion, starting material 22.8% Co/SiO_2, 1.7-mm pellet diameter, 260 $m^2\ g^{-1}$, 3.9% Co dispersion, site density = 0.51×10^{-6} g atom surface Co/m^2.

[a] $\chi = L^2\Phi\theta/r_p$; r_p in m, site density (θ) in Co atoms/m^2, L as twice the characteristic diffusion distance in m.

Increasing pellet diameter above 0.36 mm increases methane and CO_2 selectivities (Table 4). Methane selectivity increases because transport restrictions decrease intrapellet CO concentrations. At low CO concentrations, FT synthesis kinetics favor light paraffins. As a result, C_5^+ selectivity and olefin content in products decrease with increasing pellet size. Lower CO_2 selectivities observed on small (Table 4) or eggshell (Table 3) pellets apparently reflect transport-limited water removal from larger catalysts pellets. In general, CO_2 selectivity increases with increasing CO conversion and water concentration, suggesting that CO_2 forms in secondary water–gas shift reactions involving water as one of the reactants. Intrapellet water concentrations increase as large pellets slow down water removal; this leads to faster water–gas shift reactions and to higher CO_2 selectivities. CO and H_2O diffusivities in liquid hydrocarbon are similar and the FT synthesis stoichiometry requires that one water molecule be removed for each CO molecule consumed. As a result, water removal and CO arrival become limited by transport rates in the same range of pellet diameter.

Somewhat surprisingly, FT synthesis rates are not influenced strongly by pellet diameter in a size range where marked selectivity changes occur. This reflects the negative order FT synthesis kinetics in the diffusion-limited reactant (CO) (4). Such negative order kinetics delay the inevitable decrease in catalyst productivity that ultimately occurs as reactant transport limitations become more severe (Section 4.4).

Below, we describe a reaction-transport model that includes the combined effects of pellet size, eggshell thickness, and volumetric rates (site density) on FT synthesis selectivity and which suggests pellet designs leading to maximum C_5^+ yields.

4.4. Reactant Transport Models

We have previously described FT synthesis selectivity models that did not account for intrapellet reactant gradients (1, 2). These models described FT synthesis selectivity of small pellets, where slow removal of olefin products increase their role in secondary readsorption reactions. In larger pellets, CO consumption rates become limited by diffusion and lead to reactant concentration gradients that strongly influence FT synthesis selectivity and, to a lesser extent, also reaction rates (1, 3, 4).

Our reaction-transport model includes mass conservation equations accounting for the stoichiometry of two main reactions: hydrocarbon synthesis with a 2:1 (H_2:CO) consumption ratio,

$$CO + 2H_2 \rightarrow -(CH_2)- + H_2O, \qquad [3]$$

and methane formation with a (H_2:CO) consumption ratio of 3:1,

$$CO + 3H_2 \rightarrow CH_4 + H_2O. \qquad [4]$$

CO consumption and methane formation turnover rates on Co catalysts are described by kinetic expressions reported previously [3, 4]:

$$R_{CO} = \frac{k_1 P_{H_2}^{0.60} P_{CO}^{0.65}}{1 + \bar{K} P_{CO}} \qquad [5]$$

$$R_{CH_4} = \frac{k_2 P_{H_2}^{1.0} P_{CO}^{0.05}}{1 + \bar{K} P_{CO}} \qquad [6]$$

At steady-state, reactant mass balances for CO and H_2 within catalyst pellets are described by

$$\nabla D_{CO} \cdot \nabla (C_T P_{CO}/H_{CO}) - a_v R_{CO} = 0 \qquad [7]$$

$$\frac{\partial P_{CO}}{\partial r} = 0 \text{ at } r = 0; \qquad P_{CO} = P_{CO}(z) \text{ at } r = R_0 \qquad [8]$$

$$\nabla D_{H_2} \cdot \nabla (C_T P_{H_2}/H_{H_2}) - a_v R_{H_2} = 0 \qquad [9]$$

$$\frac{\partial P_{H_2}}{\partial r} = 0 \text{ at } r = 0; \qquad P_{H_2} = P_{H_2}(z) \text{ at } r = R_0, \qquad [10]$$

where C_T is the total molar concentration of the liquid phase and a_v is the surface area per unit volume within catalyst pellets. P_{CO}, D_{CO}, H_{CO} and P_{H_2}, D_{H_2}, H_{H_2} are virtual pressures (fugacities), effective diffusivities, and Henry's law constants of CO and H_2 within liquid-filled catalyst pellets, respectively.

The corresponding mass balance equations within interpellet bed voids become

$$\frac{U}{RT}\frac{dP_{CO}}{dz} = -a_p \langle R_{CO} \rangle, \qquad P_{CO}(0) = P_{CO|0}, \qquad [11]$$

$$\frac{U}{RT}\frac{dP_{H_2}}{dz} = -a_p \langle R_{H_2} \rangle, \qquad P_{H_2}(0) = P_{H_2|0}, \qquad [12]$$

where a_p is the pellet surface area per unit volume of reactor and $\langle R_{CO} \rangle$ and $\langle R_{H_2} \rangle$ are total rates of CO and H_2 consumption within a catalyst pellet located at an axial position z in a plug-flow reactor. $P_{CO|0}$ and $P_{H_2|0}$ are the reactant partial pressures at the reactor inlet. Equations (5)–(12) describe CO and H_2 intrapellet and interpellet concentrations (P_{CO}, P_{H_2}) in a plug-flow reactor. The dimensionless form of these equations can be obtained by defining the following variables and parameters:

$$x = \frac{P_{CO}}{P_0}; \qquad y = \frac{P_{H_2}}{P_0}; \qquad \zeta = \frac{r}{R_0}$$

$$\lambda = \frac{z}{H}; \quad S_{CO} = \frac{R_{CO}}{R_{CO}^*}; \qquad S_{H_2} = \frac{R_{H_2}}{R_{CO}^*}$$

$$\mathrm{Pe}_0 = \frac{UP_0/RT}{a_p H R^*_{CO}}; \quad \Phi_0^2 = \frac{R_0^2 a_v H_{CO} R^*_{CO}}{C_T P_0 D_{CO}}; \quad \gamma_0 = \frac{D_{CO}/H_{CO}}{D_{H_2}/H_{H_2}}, \quad [13]$$

$$x_0 = \frac{P_{CO|0}}{P_0}; \qquad y_0 = \frac{P_{H_{20}}}{P_0},$$

where R^*_{CO} is a reference CO rate.

These dimensionless parameters can be substituted into Eqs. [5]–[12] to give:

$$\nabla^2 x - \Phi_0^2 S_{CO} = 0 \quad [14]$$

$$\frac{\partial x}{\partial \xi} = 0 \text{ at } \xi = 0; \qquad x = x(\lambda) \text{ at } \xi = 1 \quad [15]$$

$$\nabla^2 y - \Phi_0^2 S_{H_2}/\gamma_0 = 0 \quad [16]$$

$$\frac{\partial y}{\partial \xi} = 0 \text{ at } \xi = 0; \qquad y = y(\lambda) \text{ at } \xi = 1 \quad [17]$$

$$\frac{dx}{d\lambda} = -\frac{1}{\mathrm{Pe}_0}\langle S_{CO}\rangle, \qquad x(0) = x_0 \quad [18]$$

$$\frac{dy}{d\lambda} = -\frac{1}{\mathrm{Pe}_0}\langle S_{H_2}\rangle, \qquad y(0) = y_0. \quad [19]$$

4.5. Dimensional Analysis of Model Equations and Comparisons with Experimental Results

This system of coupled boundary value problems and ordinary differential equations (Eqs. [14]–[19]) contains three key dimensionless parameters that describe the rate and selectivity of FT synthesis in plug-flow reactors: a Thiele modulus (Φ_0^2), a Peclet number (Pe_0), and a permeability factor (γ_0) containing the solubility and diffusivity of CO and H_2 reactants in molten hydrocarbon wax.

The Thiele modulus describes the relative rates of intrapellet diffusion and reaction. It can be separated into two terms (ψ_{CO} and χ)

$$\Phi_0^2 = \psi_{CO} \cdot \chi = \left(\frac{2H_{CO}R^*_{CO}}{C_T P_T D_{CO}}\right) \cdot \left(\frac{R_0^2 \Phi \theta_M}{r_p}\right), \quad [20]$$

where Φ is the pellet porosity, r_p is the mean pore radius, R_0 is the pellet radius, and θ_M is the intrapellet site density. ψ_{CO} (or ψ_{H_2} when H_2 is the diffusion-limited reactant) depends only on the solubility (H), diffusivity (D), and reactivity (R^*) of CO (or H_2); in contrast, χ depends only on structural catalyst properties. In deriving Eq. [20], we have used the definition of Φ_0^2 (Eq. [13]) and a value for a_v given by:

$$a_v = \frac{2\Phi}{r_p}, \quad [21]$$

an expression that accurately describes the specific surface area of porous solids commonly used as catalyst supports (39).

The Peclet number (Pe_0) reflects the relative rates of intrapellet diffusion and of convection within bed interstices. This parameter measures the relative importance of CO depletion within pellets, caused by diffusional restrictions, and within bed voids, caused by slow convection (low space-velocity). The parameter γ_0 reflects the relative permeabilities of CO and H_2 and determines which component becomes the diffusion-limited reactant for a given feed composition; at typical synthesis conditions (473 K), the value of γ_0 is about 1.9. Together with the reaction stoichiometry (Eq. [3]), material balances (Eqs. [14] and [16]) and H_2/CO feed ratio of 2.0–2.1, such a value of γ_0 implies that CO becomes the diffusion-limited reactant. For typical FT liquid compositions, γ_0 varies only between 1.8 to 2.0 as temperatures change between 423 and 523 K (40, 41).

The structural parameter χ was chosen as the defining catalyst property in order to compare simulations with experimental results. The remaining components in the Thiele modulus (contained within ψ_{CO} in Eq. [20]) remain unaffected by structural modifications or by nonuniform site distributions because ψ_{CO} contains only intrinsic kinetic and diffusive properties of reacting molecules. These properties are independent of site density or location and of support pore structure. For example, the site activity of exposed Co atoms depends only weakly on metal dispersion or on the chemical properties of metal oxide supports [42]. Also, the CO diffusivity through intrapellet liquids is independent of support pore diameter, because diffusion through liquid occurs predominantly by molecule–molecule interactions within the bulk liquid.

Model simulations of FT synthesis rate and methane selectivity are shown in Fig. 5 as a function of the Thiele modulus (Φ_0). The effectiveness factor, defined as the ratio of actual to kinetic-controlled reaction rates, first increases slightly as Φ_0 increases because of the negative order CO kinetics (see Eq. [5]). The model predicts that synthesis rates are only slightly influenced by increasing diffusional restrictions (Fig. 5a) in a range of Thiele moduli (Φ_0) where methane selectivity changes markedly (Fig. 5b). This behavior is consistent with the observed effect of pellet size on rate and selectivity (Table 4); the initial increase in synthesis rate as Φ_0 increases (Fig. 5a) reflects the onset of transport restrictions, which decrease intrapellet CO concentrations. The impact of negative order FT synthesis kinetics is most marked for lighter products and their formation becomes favored within transport-limited pellets. Low CO concentrations favor chain termination over chain growth and lead to the synthesis of lighter and more paraffinic products (Tables 3 and 4).

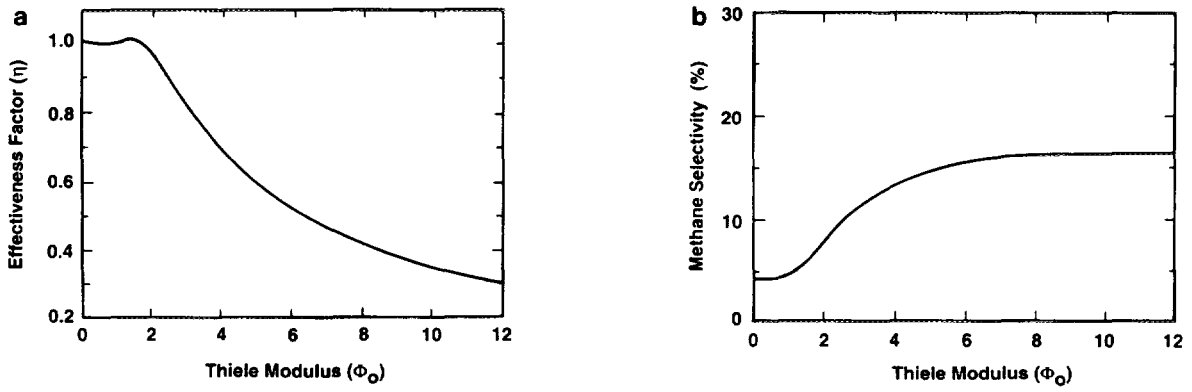

FIG. 5. The effect of catalyst Thiele modulus on Fischer–Tropsch synthesis rate and methane selectivity: Model simulations. (a) rate effectiveness factor, (b) methane selectivity (473 K, 2000 kPa, H_2/CO = 2.1, 55–65% CO conversion, >24 h on stream).

Experimental CH_4 and C_5^+ selectivities for Co supported on SiO_2, TiO_2, or Al_2O_3 powders (42) and for Co/SiO_2 eggshell and large uniformly impregnated pellets (Table 3) are shown in Fig. 6 as a function of the structural parameter χ. C_5^+ selectivity initially increases as χ increases (Fig. 6a). This occurs because reactant transport restrictions are negligible at low values of χ but the readsorption of α-olefins, a reaction that increases product molecular weight, is enhanced by the diffusion-limited intrapellet removal of such reactive molecules (1–5). Methane selectivity decreases in the same range of low χ values (Fig. 6b), also as a direct result of diffusion-enhanced α-olefin readsorption (1–4).

Ultimately, further increases in χ lead to lower C_5^+ selectivities because structural catalyst properties that control the diffusional removal of α-olefins at low values of χ begin to restrict reactant arrival rates as χ increases further (Fig. 6a). Then, methane selectivity also reverses its initial trend and increases with increasing χ. These results show that transport restrictions and the resulting changes in selectivity reflect changes in χ, independently of how the value of χ is varied. Intermediate values of χ, which limit olefin removal and enhance their secondary readsorption but still permit rapid access of reactants to reaction sites, lead to highest C_5^+ selectivities.

Reactant transport restrictions at high values of χ also lead to a decrease in activation energy, from about 125 kJ mol^{-1} on kinetic-limited (small) pellets to values of 65-75 kJ mol^{-1} on large evenly impregnated pellets (Fig. 7). This decrease in activation energy is typical of reactions limited by reactant transport. The overall pressure order increases when CO transport rates limit reaction rates (Fig. 7). This change in apparent kinetic order reflects the increasing severity of transport restric-

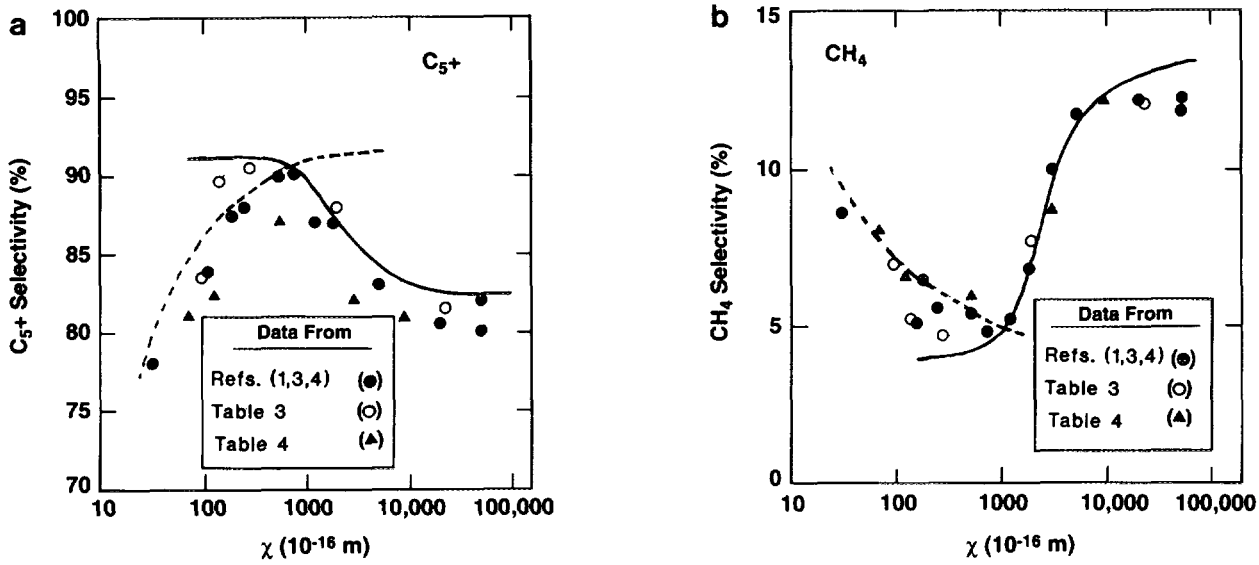

FIG. 6. The effect of catalyst structural parameter (χ) on Fischer–Tropsch synthesis selectivity: Comparison of model simulations and experimental results. (a) C_5^+ selectivity, b) methane selectivity, (473 K, 2000 kPa, H_2/CO = 2.1, 55–65% CO conversion, >24 h on stream).

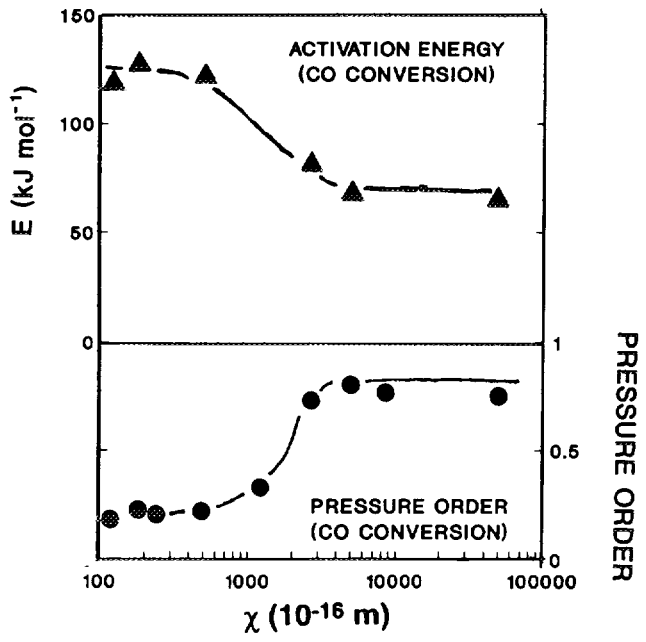

FIG. 7. The effect of catalyst structural parameter (χ) on Fischer–Tropsch synthesis activation energy and kinetics (473 K, 2000 kPa, H_2/CO = 2.1, 55–65% CO conversion, >24 h on stream).

tions as CO pressure decreases, because transport rates decrease linearly with pressure but kinetic pellet requirements decrease much less rapidly ($r \sim P_T^n$, n = 0.2–0.25).

Our reactant transport model (Eqs. [14–19]) predicts the observed decrease in C_5^+ selectivity and the concurrent increase in methane observed experimentally with increasing values of χ (Fig. 6). The solid lines in Figs. 6a and 6b show the results of simulations using literature values for CO and H_2 diffusivities and solubilities and our reaction kinetics and catalyst structure data. These simulations are in excellent agreement with the experimental results. We previously described the results for low values of χ using a model that accounts for the diffusion-enhanced readsorption of α-olefins (dashed curves in Figs. 6a and 6b) (1, 3, 4).

At low values of χ ($\chi < 500 \times 10^{-6}$ m), the *reactant* transport model (dashed curves, Figs. 6a and 6b) predicts that C_5^+ and CH_4 selectivities are not influenced by structural catalyst properties and depend only on intrinsic reaction kinetics. At higher values of χ, CO hydrogenation occurs at lower intrapellet CO concentrations within increasingly thin regions near outer pellet surfaces. Sharp CO concentration gradients (and less pronounced H_2 gradients) occur and catalytic sites near the center regions of pellets become inaccessible to CO reactants and unavailable for FT synthesis reactions. Such sites, however, may still catalyze secondary olefin hydrogenation, a reaction that occurs readily on Co when CO is not present (4, 5).

Eggshell catalysts eliminate these concentration gradients by placing Co sites within thin regions near the outer pellet surface, where CO concentrations (fugacities) are nearly uniform and identical to those in equilibrium with the surrounding interpellet gas phase. A minor change in the defining reaction-transport equations (Eqs. [14–19]) renders these equations valid for eggshell pellets with shell thickness ($R_0 - R_c$). The definition of χ for eggshell pellets simply becomes

$$\chi = (R_0 - R_c)^2\theta_M/r_p, \qquad [22]$$

where R_c is the radius of the internal nonimpregnated core. For thin eggshells ($R_c/R_0 \sim 1$), the Laplacian operator in Eqns. [14] and [16] reduces to the second derivative of the respective reactant concentrations. If the shell thickness is a significant fraction of the pellet radius, then this operator contains an additional term $[2(R_0 - R_c)/((R_0 - R_c)\xi + R_c))]$ that multiplies the first derivative. This curvature term vanishes as R_c/R_0 approaches unity.

Our experimental data (Figs. 6a and 6b) suggest that optimal design of eggshell pellets requires materials with values of χ between 200 and 2000 $\times 10^{-16}$ m. This range of structural parameters maximizes C_5^+ selectivities while maintaining FT synthesis rates near their intrinsic kinetic values.

Selectivity changes observed during deactivation are consistent with the expected decrease in the density of available sites (θ_M) as deactivation proceeds. Methane selectivity decreases as large transport-limited pellets deactivate (Fig. 8), because reactant consumption requirements decrease as sites deactivate. Deactivation decreases the required transport load and the value of χ for a given catalyst. Catalysts with χ values greater than those

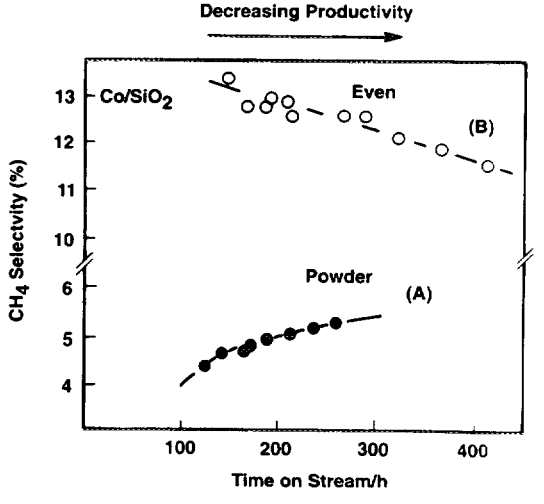

FIG. 8. The effect of catalyst deactivation on Fischer–Tropsch synthesis selectivity on large and small pellets (473 K, 2000 kPa, H_2/CO = 2.1, 55–65% CO conversion, >24 h on stream).

required for minimum methane selectivities such as the Co/SiO_2 powders in Fig. 8, show the opposite trend. On these catalysts, methane selectivities increase as deactivation proceeds (Fig. 8) because intrapellet α-olefin concentrations also decrease with decreasing site density.

Several catalyst properties are available to modify the structural parameter χ (Eqs. [20] and [22]). The eggshell thickness ($R_0 - R_c$) is an obvious choice because it determines the distance that reactants must diffuse to reach catalytic sites. Catalyst pellet diameter ($2R_0$), which controls pressure drop in packed-bed reactors, and pellet diffusion length, which controls intrapellet transport rates, can be varied independently only by using eggshell catalysts. Other catalyst properties, such as porosity (Φ) and pore radius (r_p), can also be used in pellet design. Increasing catalyst porosity leads to higher void volumes available for transport. Intrapellet transport restrictions become more severe within smaller pores, not because reactant or product diffusivities are lower, but because the number of sites per unit volume increases with decreasing pore size for a given site density. The product of the metal site density (θ_M) and the surface area per unit volume (a_v) defines the volumetric productivity of catalyst pellets, and therefore the transport load required to satisfy the intrinsic reactant requirements within a given catalyst volume. Thus, pellets with higher site densities require that such sites be placed closer to the outer pellet surface.

Transport restrictions can be lessened by the use of less active catalysts, a solution that also increases required reactor volumes in industrial practice. Thus, the ability to prepare sharp concentration profiles of active sites near outer pellet surfaces remains a very attractive solution to relieve transport restrictions in packed-bed FT synthesis reactors. Interestingly, our model predicts that maximum FT synthesis *rates* actually occur on pellets slightly limited by CO diffusion (Fig. 5a), a clear consequence of the negative CO order reaction kinetics. As a result, optimum FT synthesis *rates* require egg-yolk rather than eggshell pellets, a conclusion previously reached for other negative order reactions (43). Thus, when highest C_5^+ synthesis rates (i.e., the product of total rate and C_5^+ selectivity) are desired, FT synthesis pellets should contain bands of active sites at intermediate radial positions within pellets.

4.6. The Design and Synthesis of Large Fischer–Tropsch Catalyst Pellets

In a process such as FT synthesis, where transport limitations are ubiquitous and often unavoidable, even in laboratory reactors, we obtain an unexpected benefit from catalyst design options introduced by structural parameters; these options are unavailable in kinetic-limited pellets. Site activity (turnover rate) and chain growth kinetics appear to be intrinsic properties of Co surface ensembles and depend weakly on site modifications introduced by changes in Co crystallite size or in metal oxide support (42). Changes in synthesis rate and selectivity occur when Co is alloyed with another metal but they reflect changes in Co dispersion, site density and stability, or reducibility, instead of modifications in intrinsic surface chemistry (44–48). Thus, the intrinsic behavior of Co-based FT synthesis catalysts is difficult to control by modifying impregnation or pretreatment procedures or by choosing a different support. Transport restrictions become one of the few selectivity modifiers available for the design of Ru- and Co-based FT synthesis catalysts, where carbon number distributions are additionally constrained by polymerization chain growth kinetics.

Catalyst pellets that remove all transport restrictions actually give low C_5^+ selectivities (Fig. 6a) because they decrease intrapellet α-olefin concentrations and limit their involvement in beneficial secondary readsorption and chain initiation reactions. Structural catalyst properties that restrict intrapellet α-olefin transport lead to highest C_5^+ selectivities. They also allow the effective introduction of other secondary olefin reactions (hydrogenation, hydroformylation, cracking) to modify selectivity in bifunctional catalyst pellets (3, 4).

Optimum catalysts, in fact, behave as porous catalytic membranes that selectively retain larger olefin products, but which maintain fast reactant transport within pellets. The permeability of such a catalytic membrane can be modified by changing its thickness (i.e., the width of the catalytic region in a pellet) or the liquid viscosity and molecular weight (e.g., by extensive product recycle in FT synthesis (49)), changes that move χ and catalytic behavior along the curves shown in Fig. 6. Changes in permeability do not alter the shape of these curves because they affect both reactants and product diffusion rates; modifications of permeation selectivity, in contrast, change the shape of these curves and broaden or narrow the range of χ values leading to maximum C_5^+ yields.

Selective inhibition of olefin transport moves the left side of Fig. 6, a region where olefin transport is the primary modifier of catalytic selectivity, farther to the left; it does not, however, affect catalysts with values of χ greater than χ_{max}, where selectivity changes occur only because of reactant transport restrictions. Similarly, the selective enhancement of CO transport rates without changes in olefin diffusivity moves the right side of such curves farther to the right and broadens the χ region where highest C_5^+ values are obtained. Enhanced CO transport apparently occurs as the concentration of water (an indigeneous product of FT synthesis) increases with axial position in packed-bed reactors. This effect may account for the higher C_5^+ selectivity (50, 51) and reaction rates (51) obtained when water is introduced along with synthesis gas into FT synthesis reactors. More subtle effects

can be introduced by varying the relative permeation selectivity of the liquid phase for the two reactants (CO and H_2). Then, stoichiometric ratios can be maintained near intrapellet sites even when feed (H_2/CO) ratios differ significantly from the stoichiometric consumption ratio. Detailed descriptions of these design options are beyond the scope of the present study, which describes only the required tools for the design of Co-based catalysts for selective synthesis of C_5^+ products in FT synthesis.

5. CONCLUSIONS

We have developed a new impregnation technique for preparing eggshell catalyst pellets. This technique exploits the capillary-driven imbibition of a molten metal salt into mesoporous oxide supports. We have applied this technique successfully to prepare Co-based eggshell catalysts for the FT synthesis. These eggshell catalysts temper diffusional restrictions that normally lead to low reaction rates and C_5^+ selectivities on large pellets required in packed-bed reactors. Synthesis rates and C_5^+ selectivities on eggshell catalysts with sharp 0.1–0.2 mm impregnated regions near outer pellet surfaces are similar to, and sometimes even higher, than on uniformly impregnated catalyst powders (<0.2 mm diameter). The imbibition models and the synthetic procedures that we report here can also be applied to the synthesis of other nonuniformly impregnated catalytic materials, where weak impregnant-support interactions and high local site density requirements preclude the use of conventional synthesis and pretreatment techniques.

APPENDIX: NOMENCLATURE

a_p	Surface area per unit reactor volume
a_v	Surface area per unit volume of catalyst particle
C_T	Molar concentration of liquid phase
D_{CO}	Effective diffusivity of CO within catalyst particle
D_{H_2}	Effective diffusivity of H_2 within catalyst particle
H	Reactor length
H_{CO}	Henry's constant for CO
H_{H_2}	Henry's constant for H_2
k_1	Kinetic constant for CO consumption
k_2	Kinetic constant for CH_4 formation
$\overline{K}$	CO adsorption constant
P_{CO}	CO partial pressure
$P_{CO\|0}$	CO partial pressure at reactor inlet
Pe_0	Peclet number
P_{H_2}	H_2 partial pressure
$P_{H_2,0}$	H_2 partial pressure at reactor inlet
P_T	Total pressure
r	Catalyst pellet radial dimension
R	Universal gas constant
R_c	Radius of internal core without catalytic sites
R_{CH_4}	Local rate of CH_4 formation
R_{CO}	Local rate of CO consumption
R_{H_2}	Local rate of H_2 consumption
$\langle R_{CO} \rangle$	Particle-integrated rate of CO consumption
$\langle R_{H_2} \rangle$	Particle-integrated rate of H_2 consumption
R_{CO}^*	Reference rate of CO consumption
R_0	Catalyst pellet radius
r^*	Liquid penetration depth
r_p	Mean pore radius
S_{CO}	Dimensionless rate of CO consumption
S_{H_2}	Dimensionless rate of H_2 consumption
$\langle S_{CO} \rangle$	Particle-integrated dimensionless rate of CO consumption
$\langle S_{H_2} \rangle$	Particle-integrated dimensionless rate of H_2 consumption
t	Impregnation time
T	Absolute temperature
U	Interstitial gas velocity
x	Dimensionless CO concentration
y	Dimensionless H_2 concentration
z	Axial reactor distance

Greek Symbols

γ	Surface tension of impregnating solution
γ_0	CO/H_2 effective permeability ratio
ζ	Dimensionless penetration depth
θ	Contact angle between impregnating solution and pore surfaces
θ_M	Catalyst site density
λ	Dimensionless reactor position
μ	Viscosity of impregnating solution
ξ	Dimensionless pellet position
Φ	Pellet porosity
Φ_0^2	Thiele modulus
χ	Structural parameter defined in Eq. [20]
ψ_{CO}	Diffusivity/reactivity parameter defined in Eq. [20]

ACKNOWLEDGMENTS

We thank Dr. Rocco A. Fiato for many helpful discussions and Ms. Hilda Vroman and Mr. Bruce DeRites for the synthesis, characterization, and catalytic evaluation of some of the materials discussed in this work. We also thank Dr. Eric Herbolzheimer and Ms. Dee Redd for the viscosity and surface tension measurements.

REFERENCES

1. Iglesia, E., Reyes, S. C., and Madon, R. J., *J. Catal.* **129,** 238 (1991).
2. Madon, R. J., Reyes, S. C., and Iglesia, E., *J. Phys. Chem.* **95,** 7795 (1991).

3. Iglesia, E., Reyes, S. C., and Soled, S. L., *in* "Computer-Aided Design of Catalysts and Reactors" (Becker, E. R. and Pereira, C. J., Eds.) p. 199. Dekker, New York, 1993.
4. Iglesia, E., Reyes, S. C., Madon, R. J., and Soled, S. L., *in* "Advances in Catalysis and Related Subjects" (Eley, D. D., Pines, H., and Weisz, P. B., Eds.) Vol. 39, p. 239. Academic Press, New York, 1993.
5. Madon, R. J., Reyes, S. C., and Iglesia, E., *in* "Selectivity in Catalysis," ACS Symposium Series (Suib, S. L. and Davis, M. E., Eds.). Am. Chem. Soc., Washington, DC, 1992.
6. Maatman, R. W., and Prater, C. D., *Ind. Eng. Chem.* **49,** 253 (1957).
7. Corbett, W. E., and Luss, D., *Chem. Eng. Sci.* **29,** 1473 (1974).
8. Pereira, C. J., Kim, G., and Hegedus, L. L., *Catal. Rev. Sci. Eng.* **26,** 583 (1984); Summers, J. E., and Hegedus, L. L., *J. Catal.* **51,** 185 (1978).
9. Fischer, F. and Tropsch, H., *Brennst. Chem.* **7,** 97 (1926); Fischer, F., and Koch, H., *Brennst. Chem.* **13,** 61 (1932); Fischer, F., *Brennst. Chem.* **16,** 6 (1935).
10. Anderson, R. B., Seligman, B., Schultz, J. F., Kelly, R., and Elliott, M. A., *Ind. Eng. Chem.* **44,** 391 (1952).
11. Madon, R. J., Bucker, E. R., and Taylor, W. F., ERDA (DOE) Report No. E(46-1), 1977.
12. Bub, G. and Baerns, M., *Chem. Eng. Sci.* **35,** 348 (1980).
13. Stern, D., Bell, A. T., and Heinemann, H., *Chem. Eng. Sci.* **40,** 1655 (1985); *Chem. Eng. Sci.* **40,** 1917 (1985).
14. Zimmerman, W. H., Rossin, J. A., and Bukur, D. B., *Ind. Eng. Chem.* **28,** 406 (1989).
15. Dixit, R. S., Ph.D. dissertation, Illinois Institute of Technology, 1980.
16. Dixit, R. S. and Tavlarides, L. L., *Chem. Eng. Sci.* **37,** 539 (1982); *Ind. Eng. Chem. Proc. Des. Dev.* **22,** 1 (1983).
17. Post, M. F. M., van't Hoog, A. C., Minderhoud, J. K., and Sie, S. T., *AIChe J.* **35,** 1107 (1989).
18. Sie, S. T., Senden, M. M. G., and Van Wechem, H. M. H., *Catal. Today* **8,** 371 (1991).
19. Behrmann, W. C., Mauldin, C. H., Arcuri, K. B., and Herskowitz, M., Eur. Pat. Appl. 266,898 (1988).
20. Everson, R. C., Woodburn, E. T., and Kirk, A. R. M., *J. Catal.* **53,** 186 (1978).
21. van Erp, W. A., Nanne, J. M., and Post, M. F. M., U.S. Patent 4,637,993 (1987); Eur. Pat. Appl. 178,008 (1986).
22. Post, M. F. M., and Sie, S. T., Eur. Pat. Appl. 174,696 (1986).
23. Post, M. F. M., and Sie, S. T., Eur. Pat. Appl. 167,215 (1986); U.K. Patent 2,161,177 (1986).
24. Mauldin, C. H., and Riley, K. L., U.S. Patent 4,977,126 (1990).
25. Iglesia, E., Vroman, H., Soled, S. L., Baumgartner, J. E., and Fiato, R. A., U.S. Patent 5,036,032 (1991); Eur. Pat. Appl. 313,466 (1991).
26. Karn, F. S., Shultz, J. F., and Anderson, R. B., *Ind. Eng. Chem. Product Res. Dev.* **4,** 265 (1965).
27. Kasaoka, S., and Sakata, Y., *J. Chem. Eng. Jpn.* **1,** 138 (1968).
28. Smith, T. B., *Ind. Eng. Chem. Proc. Des. Dev.* **15,** 388 (1976).
29. Carberry, J. J., *Chim. Industr.* **51,** 951 (1969).
30. Minhas, S., and Carberry, J. J., *J. Catal.* **14,** 270 (1969).
31. Smith, T. G., and Carberry, J. J., *Can. J. Chem. Eng.* **53,** 347 (1975).
32. Lee, S-Y. and Aris, R., *Catal. Rev.-Sci. Eng.* **27,** 207 (1985).
33. Kunimori, K., Kawasaki, E., Nakajima, I., and Uchijinama, T., *Appl. Catal.* **22,** 115 (1986).
34. Roth, J. F. and Richard, T. E., *J. Res. Inst. Catal. Hokkaido Univ.* **20,** 85 (1972).
35. Innes, W. B., *in* "Experimental Methods in Catalytic Research" (R. B. Anderson, Ed.), p. 45. Academic Press, New York/London, 1968.
36. Wasburn, E., *Phys. Rev.* **17,** 273 (1921).
37. Iglesia, E., Soled, S. L., and Fiato, R. A., U.S. Patent 4,738,948 (1988); Eur. Patent Appl. 363,537 (1988).
38. Iglesia, E., Vroman, H., Soled, S. L., and Baumgartner, J. E., Eur. Pat. Appl. 434,284 (1991).
39. Reyes, S. C., and Iglesia, E., *J. Catal.* **129,** 457 (1991).
40. Matthews, M. A., Rodden, J. B., and Akerman, A., *J. Chem. Eng. Data.* **32,** 319 (1987).
41. Albal, R. S., Shah, Y. T., Carr, N. L., and Bell, A. T., *Chem. Eng. Sci.* **39,** 905 (1984).
42. Iglesia, E., Soled, S. L., and Fiato, R. A., *J. Catal.* **137,** 212 (1992).
43. Becker, E. R., and Wei, J., *J. Catal.* **46,** 365 (1977).
44. Kobylinski, T., Kibby, C. L., Pannell, R. B., and Eddy, E. L., U.S. Pat. 4,605,676 (1986).
45. W. C. Behrmann and C. H. Mauldin, Eur. Pat. Appl. 266,898 (1987); C. H. Mauldin, U.S. Pat. 4,568,663 (1986).
46. Iglesia, E., Soled, S. L., and Fiato, R. A., U.S. Pat. 4,822,824 (1989); U.S. Pat. 4,738,948 (1978); Eur. Pat. Appl. 319,625 (1989).
47. Goodwin, J., Marcelin, G., Eri, G., and Rils, T. Eur. Pat. Appl. 313375 (1988).
48. Iglesia, E., Soled, S. L., Fiato, R. A., and Via, G. H., *J. Catal.* **143,** 345 (1993).
49. Yokota, K., Hanakata, Y., and Fujimoto, K., *Chem. Eng. Sci.* **45,** 2743 (1990); Yokota, K., and Fujimoto, K., *Fuel* **68,** 255 (1989).
50. Minderhoud, J. K., Post, M. F., and Sie, S. T., Eur. Pat. Appl. 109,702 (1984).
51. Kim, C. J., Eur. Pat. Appl. 339,923 (1989).